

Detection of 27 Candidate Circumbinary Planets Through Apsidal Precession of Eclipsing Binaries Observed by TESS

Margo Thornton ^{1,2} Benjamin T. Montet ¹ Riley White,¹ Arden Shao ³ and Diya T. Kumar³

¹*School of Physics, University of New South Wales, Kensington NSW 2052, Australia*

²*The SETI Institute, 339 N Bernardo Ave Suite 200, Mountain View, CA 94043, United States*

³*Cahill Center for Astronomy and Astrophysics, California Institute of Technology, 1200 E. California Blvd., MC 249-17, Pasadena, CA 91125, United States*

10 December 2025

ABSTRACT

Most circumbinary planets have been discovered by their transits, limiting our understanding of such systems to those with mutually coplanar architectures. This bias makes it difficult to infer the true circumbinary planet population, highlighting the need for alternative detection methods that do not rely on transits. In this work, we explore one such approach by leveraging apsidal precession as a dynamical signature of planetary companions. We analyse TESS photometry of a sample of 1,590 eclipsing binaries from the Gaia DR3 Catalogue of Eclipsing Binary Candidates to identify systems exhibiting detectable apsidal precession. We rule general relativistic, tidal, and rotational contributions as insufficient to account for the measured apsidal precession, demonstrating that an additional gravitational perturber is required. This enables us to constrain the possible masses and orbital separations of a companion that would cause the observed precession. We present a new set of 27 candidate circumbinary planets identified through this precession-based method as well as 6 candidate companions with a higher minimum mass. Their inferred properties remain degenerate, as the same dynamical signatures can arise from lower-mass planets at less than 1 AU or from more massive companions on wider, few-AU orbits, reflecting the current uncertainty in characterising these systems. Radial velocities can help break this degeneracy and provide direct confirmation.

Key words: binaries: eclipsing – exoplanets – eclipses – methods: data analysis, observational – planets and satellites: detection

1 INTRODUCTION

The existence of circumbinary planets, exoplanets that orbit binary stars, has been confirmed in just the last 15 years (Doyle et al. 2011). NASA’s Kepler (Borucki et al. 2010) and TESS (Ricker et al. 2015) missions have enabled the discovery of 14 circumbinary planets (CBPs) via transits (e.g. Welsh et al. 2012; Orosz et al. 2012b; Schwamb et al. 2013). All of these confirmed systems are transiting CBPs, detected because their orbital planes are closely aligned with that of the binary. These are highly reliable detections because of their distinctive transit signatures. However, relying primarily on transits may bias our current understanding of CBPs toward coplanar and compact systems, leaving a potentially large population of wider or misaligned planets undetected. Despite its all-sky coverage, TESS has revealed only two CBPs (Kostov et al. 2020, 2021), further illustrating the difficulty of detecting these planets through transits alone. The BEBOP Survey (Martin et al. 2019) has revealed 2 CBPs via the radial velocity (RV) method (Standing et al. 2023; Baycroft et al. 2025). Eclipse timing variations (ETVs, Goldberg et al. 2023) and gravitational microlensing (Bennett et al. 2016) have each led to widely accepted identifications of a circumbinary planet around a main-sequence binary. A vast majority of the known CBPs are coplanar with and exist just outside the critical stability radius (r_{crit} , Holman & Wiegert 1999) of their host binary, portrayed in Figure 1; the critical radius defines the boundary for stable orbits. Although theory predicts these trends (Foucart & Lai 2013; Pierens & Nelson 2013), the search methods used so far are strongly biased toward

detecting coplanar CBPs near the inner stability boundary. Transit surveys preferentially find planets whose orbits are nearly edge-on and aligned with the binary, because even a degree of mutual inclination dramatically reduces the probability of detecting repeated transits (Martin & Triaud 2015). Similarly, planets orbiting just outside the stability radius produce frequent and more easily detectable transits, while planets at wider separations transit rarely or not at all over a mission baseline. This selection effect, along with the small sample size, emphasises the importance of developing new methods to find CBPs.

These observational biases are especially problematic because theoretical predictions for circumbinary planet formation are widely divergent. Some models suggest that circumbinary disks damp inclinations and produce highly coplanar planets (Foucart & Lai 2013). Others predict that the binary can disturb the disk, causing it to warp or become turbulent, which may tilt planetary orbits or suppress planet growth (Abod et al. 2022; Franchini et al. 2019; Chen et al. 2019). Without a representative sample, including misaligned or wide-orbit CBPs, we cannot distinguish between these competing scenarios, nor can we assess whether planet formation around binaries is more or less efficient than around single stars. This question has broader implications: microlensing surveys hint that some free-floating planets may originate from circumbinary disks through dynamical ejection (e.g. Coleman 2024; Chen et al. 2024), meaning that the efficiency of circumbinary planet formation contributes to the overall population of unbound planets. Altogether, these uncertainties highlight the need for less biased, dynamically informed

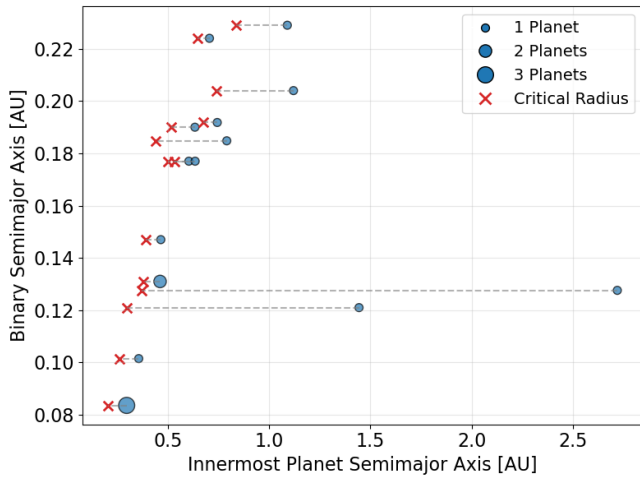


Figure 1. The distribution of the semimajor axis of the known CBPs around main sequence binaries with reference to the critical stability radius of the binary (red “x”). For the multiple planet systems, Kepler-47 (Orosz et al. 2012a) and TOI-1338 (Kostov et al. 2020; Standing et al. 2023), only the innermost planet is shown with the size of the circle corresponding to the number of planets in the system. The CBP discovered via microlensing (Bennett et al. 2016) has been omitted from this diagram due to its imprecise orbital parameter determinations. In a vast majority of the systems, the innermost planet exists just outside of the critical radius.

detection methods capable of revealing the full diversity of circumbinary planetary systems.

In Kostov et al. (2021), the authors present evidence that the argument of periastron, ω of the binary star is precessing over time, a motion attributed to the gravitational influence of a CBP that was initially detected via its transits. This effect is known as apsidal precession (due to the motion of the line of apsides), and can be caused by a third body in the system perturbing the orbit of the inner binary (Harrington 1968). Because apsidal precession corresponds to a nonzero $\dot{\omega}$, it leads to a time-varying geometry of the orbit. In an eccentric binary, the relative timing of the primary and secondary eclipses encodes the quantity $e \cos \omega$ (e.g. Hilditch 2001), so a changing ω causes $e \cos \omega$ to vary as well. This variation produces a measurable shift in the interval between successive primary and secondary eclipses, providing a direct way to detect apsidal precession. The phase difference between the primary and secondary eclipse can be represented using ω , the angle between periastron and the reference plane (ascending node), measured in the direction of the orbiting star’s motion within the orbital plane. Thus, if $\dot{\omega} \neq 0$, the primary and secondary eclipse times drift away from a strictly periodic ephemeris, resulting in a pattern where the primary eclipses and secondary eclipses diverge. With enough data covering a long time interval, the residuals are roughly sinusoidal, where a full apsidal period is the time it takes for ω to change by 360° . For the kinds of systems considered here, the apsidal periods are typically on the order of decades; for example, the system analysed by Kostov et al. (2021) has an apsidal period of roughly 50 years.

A distant companion is not the only possible cause of precession to a binary star. Effects due to general relativity (GR) and the tides and rotation of the stars can contribute to the precession (e.g. Einstein 1916; Cowling 1938; Sterne 1939). These effects are more prominent for high-mass and short-period binaries, respectively. Importantly, the magnitudes of GR and tidal/rotational precession can be calculated precisely when the stellar and orbital parameters are

known (e.g. Gimenez 1985). This allows the expected precession from these mechanisms to be separated from any additional precession induced by a third body in a wider orbit, which we explore in more detail in the analysis that follows.

Apsidal precession is a common dynamical phenomenon observed in a wide range of systems. Many hierarchical stellar triples show measurable apsidal motion driven by the outer companion (Mazeh & Shaham 1979), and even within our own Solar System, Mercury’s orbit precesses at a rate of 43 arcseconds per century due to general relativity (Einstein 1916) and precesses because of other bodies in the Solar System by 500 arcseconds per century. These examples highlight how sensitive apsidal motion is to external perturbations, making it a powerful tool for identifying and characterising CBPs.

In this work, we use the detection of apsidal precession in a binary to infer the presence of a third body orbiting the inner binary. Historically, this technique has been difficult to apply because long baselines of precise, continuous eclipse timing have rarely been available. TESS now provides multi-year, high-cadence photometry for tens of thousands of eclipsing binaries, enabling the detection of coherent apsidal motion that would have been unmeasurable in earlier surveys. Given that TESS has found only two CBPs via transits, exploiting its time-domain precision to search for dynamical signatures such as apsidal precession offers a timely and complementary pathway for expanding the CBP population.

In the sections that follow, we outline our approach to identifying and characterising precessing eclipsing binaries. Section 2 describes the data we use (§2.1), the data processing steps (§2.2), our determination of precise binary periods (§2.3), the extraction of eclipse times (§2.4), and refining the EB sample for precession analysis (§2.5). We then present our calculation of apsidal precession rates (§2.6) and the resulting constraints on potential third bodies (§2.7). Section 3 introduces the sample of circumbinary planet candidates uncovered by this method, and in Section 4 we discuss their implications and prospects for future work before concluding in Section 5.

2 METHODS

2.1 Data

Starting with the Gaia DR3 catalogue of eclipsing binary candidates (Mowlavi et al. 2023), we select a sample of targets to investigate for signs of precession. The initial selection criterion, is as follows: parallax > 1 mas, $m_G < 18$, non-ellipsoidal, main-sequence stars, and available TESS light curve data (with at least a two year baseline). From here, we apply the following analysis to the EBs with processed light curve data from MIT’s Quick-Look Pipeline (QLP, Huang et al. 2020).

2.2 Data Processing

For each target, we retrieve all available TESS QLP light curves using *lightcurve* (Lightcurve Collaboration et al. 2018). We use only data points without any quality flags applied (i.e. *QUALITY* = 0), ensuring that our analysis is restricted to measurements free of known spacecraft or pipeline anomalies. This conservative filtering avoids contamination from scattered light, cosmic rays, or other events that could mimic or distort eclipse features. After stitching the downloaded light curves across all available sectors, we assess the background level of each datum using the *sap_bkg* values. We remove data points whose background is more than 3σ from the mean, which

reduces contamination effects. Next, we remove flares and other positive outliers using one-sided sigma clipping. We do not apply lower clipping in order to preserve the eclipses.

Because QLP systematics are strongly sector-dependent, we flatten each sector individually. To do so, we (1) compute a sector-specific Box-Least Squares (BLS, Kovács et al. 2002) to locate the primary eclipse, (2) mask the primary eclipse and perform a second BLS on the remaining data to locate the secondary eclipse, (3) generate a combined eclipse mask, then (4) apply a sliding-window flattening, which removes long-term trends while preserving the eclipses. Flattening each sector avoids injecting discontinuities at sector boundaries and ensures consistent baseline normalisation before phase folding. Finally, we concatenate the flattened sectors to produce a single detrended light curve.

2.3 Finding Periods

In order to detect any variations in the eclipse timing, we must first measure the binary period. Thus, we start by using the BLS method to extract the power spectrum from the light curve. The period at maximum power gives us a good initial estimate. However, this does not allow for analysis of the primary and secondary eclipses individually, which is key to detecting precession. Therefore, we must find the period of the primary eclipses separately from the secondary eclipses. To do so, we mask out the primary eclipses based on the initial period guess and run `transitleastsquares` (TLS, Hippke & Heller 2019) on a tighter period constraint to obtain a more precise period value for the secondary eclipses. We then repeat the same process, this time masking out the secondary eclipses, to obtain a precise period of the primary eclipses. Any deviation in these two periods would indicate precession. For EBs with periods shorter than 3 days, we mark it as “short-period” and refrain from calculating precession effects of that binary. Tidal effects scale as $(a/R)^5$, where a is the semimajor axis of the binary and R is the radius of a given star in the system; thus, short-period EBs are more prone to tidal and rotational effects, and their light curves often entail more variation.

To make sense of the two period values, we can visually inspect the folded eclipses on both periods to detect any variation, as seen through an EB in our sample in Figure 2. Precession will appear if the primary eclipse phased on the primary period lines up well, whereas the secondary eclipse phased on the same period does not: the secondary eclipses will appear to occur earlier or later in time. The opposite effect will occur for the light curve folded on the secondary period. In addition to detecting precession, this step provides several auxiliary benefits. It allows us to verify that the derived periods are correct and also reveals astrophysical features such as flares, variable eclipse depths, starspot modulation, or out-of-eclipse variability. While visual inspection may not always be sufficient to catch signs of precession, especially when looking through a large sample, it serves as an essential early diagnostic to validate the robustness of the period determination before proceeding to more quantitative analyses.

2.4 Measuring Eclipse Times

In addition to looking for visual cues of precession in the light curve, we must also quantitatively analyse the mid-eclipse times to characterise the structure of the ETVs, determining whether they follow a simple linear trend or exhibit more complex variations indicative of apsidal precession or other dynamical effects.

We calculate the eclipse times using four different methods. The

first method obtains the time at half-depth of each eclipse during ingress and egress and uses the midpoint of the two as the mid-eclipse time. This approach is simple and works well for symmetric eclipses with minimal noise, but can be biased if the eclipse shape is distorted. The second method folds each eclipse at trial midpoints. We determine the mid-eclipse time as the midpoint that best aligns ingress and egress when folded. This technique is particularly useful when small variations in eclipse depth or shape exist between cycles. The third method models the phase-folded primary and secondary eclipse with SciPy’s `LSQUnivariateSpline` interpolator (Virtanen et al. 2020). We compare the eclipse model to each corresponding eclipse in the dataset. By sliding the model along the eclipse at small increments, we determine the shift that best matches the data to the model. This method is effective at capturing subtle shifts in eclipse timing even in the presence of noise or asymmetries caused by starspots or other stellar activity. The fourth method is a similar process to the previous, but instead of modelling the full eclipse, we only model the ingress and egress, then take the midpoint of the best-fitting shift for each model. This approach is advantageous when the eclipse bottoms are distorted or affected by depth variations, as it relies on the more stable ingress and egress regions rather than the variable central portion of the eclipse. By employing multiple methods, we can cross-check eclipse times, identify outliers, and ensure robust measurements under a variety of observational and astrophysical conditions.

To calculate uncertainty on the fitted eclipse midpoint, we use `lmfit` (Non-Linear Least-Squares Minimization and Curve-Fitting for Python, Newville et al. 2025; Levenberg 1944; Marquardt 1963). This tool uses a constrained least-squares optimisation. We first define the eclipse time as a free parameter within an allowed interval centered on the predicted mid-eclipse time, ensuring that the fit remains physically plausible while still permitting deviations driven by the data. The parameter and its bounds are passed to the `lmfit` minimiser, together with the residual function and the observational time series, where the flux uncertainty is approximated by the standard deviation of the out-of-eclipse data. The minimiser then performs a Levenberg–Marquardt (Levenberg 1944; Marquardt 1963) least-squares fit, varying only the eclipse time to identify the value that minimises the residuals between the observed and modelled light curve. Upon convergence, we calculate the covariance matrix of the solution with `lmfit`, from which the formal 1σ uncertainty on the eclipse time is derived. This value, reported as `stderr`, represents the propagated uncertainty derived from the local curvature of the χ^2 function at the best-fitting parameter value. We consider the uncertainties determined with this method reasonable because they account for the observed scatter in the out-of-eclipse flux and reflect the sensitivity of the fit to shifts in eclipse timing. Tests with synthetic and real data show that `stderr` closely matches the scatter in recovered mid-eclipse times, giving us confidence that the reported uncertainties accurately represent the true timing precision.

With the observed eclipse times, we compare each with the expected eclipse time calculated on the basis of a common period (the average of the primary and secondary eclipse periods). The difference between these two values, the Observed minus Calculated (O-C), is shown for the primary and secondary eclipses of an EB in our sample in Figure 3. Because we determine eclipse times using four different methods, we select the method for each system that minimises the scatter in the O-C eclipse times. Specifically, we use the method that produces the lowest weighted root-mean-square (RMS) of the O-C residuals. If the inferred period of the primary and secondary eclipses based on these eclipse times are different and we see two diverging lines, as in Figure 3, we flag it as a precessing system. If

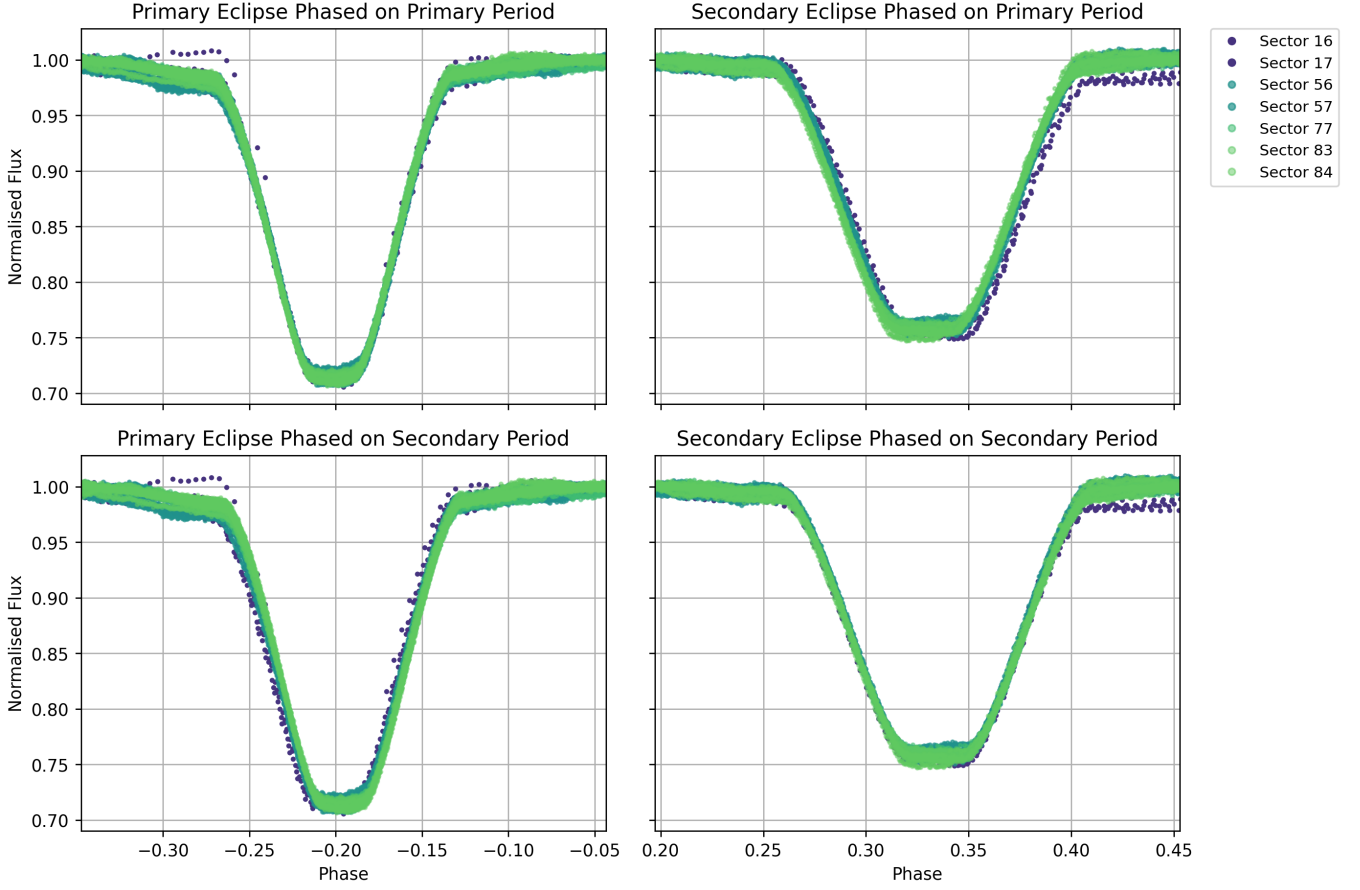


Figure 2. The phase-folded light curve of TIC 343127696, a ~ 4.67 -day eclipsing binary, showing seven sectors (~ 5 years) of data. The primary eclipses are in the left two panels, while the secondary eclipses are in the right two panels. On top, the light curve has been folded on the period of the primary eclipses while on the bottom, it has been folded on the period of the secondary eclipses. When folded on the primary period, only the primary eclipses align cleanly; when folded on the secondary period, only the secondary eclipses align clearly. This systematic offset between the two eclipse types demonstrates that their inferred periods differ, which is direct evidence of apsidal precession in the binary.

one eclipse type appears to occur earlier over time while the other appears to occur later at relatively the same rate, we know the argument of periastron must be precessing.

2.5 Refining the EB Sample for Precession Analysis

The initial cuts described in Section 2.1 reduce the full set of ~ 2 million TESS EBs to 12,819 systems suitable for further analysis. To identify those amenable to precession measurements, we apply several additional filters. First, because the typical EB period is ~ 2.5 days (Prša et al. 2011), many systems fall below the timescale where dynamical precession from a third body can be cleanly distinguished from tidal and rotational effects. We therefore exclude all binaries with orbital periods shorter than 3 days, removing 7,904 systems and leaving 4,915 longer-period EBs. Next, we require a minimum of two primary and two secondary eclipses to obtain a reliable precession rate and to avoid aliasing in the O-C signal. Also, automated period and eclipse timing determinations fail in cases due to instrumental and astrophysical variabilities in the light curves. To identify these systems, we perform a visual inspection to confirm the cause. EBs are excluded when their light curves display large out-of-eclipse modulations (e.g. strong starspots, pulsations, flares, ellipsoidal variation, instrumental noise, contamination) that prevent a stable and

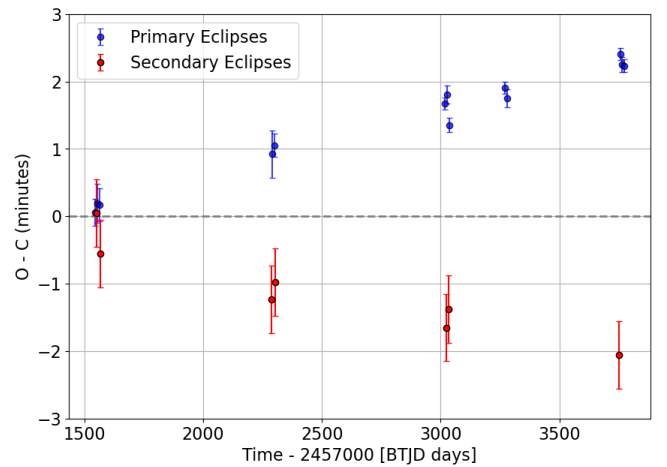


Figure 3. The observed minus calculated (O-C) plot based on a common period for TIC 286310830, a ~ 8.37 -day eclipsing binary. The primary eclipses in blue are occurring later over time while the secondary eclipses in red occur earlier than expected. This divergence in eclipse timing is a sign that the system is precessing.

repeatable mid-eclipse measurement. This step relies on by-eye vetting because the variability morphologies are diverse and not well captured by a single quantitative metric. A total of 3,325 EBs fail these requirements.

After applying these criteria, 1,590 EBs remain as our “clean” sample for initial O-C inspection. From these systems, we identify 71 binaries that show clear signatures of apsidal precession, for which we perform the full precession rate calculation and dynamical inference presented in 2.6 and 2.7.

2.6 Calculating Precession

From the pool of precessing EBs, we quantify the precession, following Charbonneau et al. (2005), starting with the calculation of $e \cos \omega$:

$$e \cos \omega = \frac{\pi}{2P} (t_I - t_{II} - \frac{P}{2} + N\Delta P) \quad (1)$$

where P is the average period of the eclipses, t_I is a mid-primary eclipse time, t_{II} is a mid-secondary eclipse time, and N is the number of cycles between the eclipses. We calculate this value with two consecutive eclipses, so the last term goes to zero. Next, we calculate $e \sin \omega$, again following Charbonneau et al. (2005):

$$e \sin \omega \approx \frac{\Theta_1 - \Theta_2}{\Theta_1 + \Theta_2} \quad (2)$$

where Θ_1 and Θ_2 are the widths of the primary and secondary eclipses, respectively. The widths are measured by eye based on the total duration of the eclipse from the start of ingress to the end of egress. This expression implicitly assumes that eclipse durations depend primarily on orbital geometry through ω , but in practice they also depend on the impact parameter (or inclination) of each eclipse. Because we do not model the impact parameter explicitly, our estimates of $e \sin \omega$ carry additional systematic uncertainty. As a result, $e \cos \omega$ is significantly better constrained than $e \sin \omega$, which we highlight as the dominant source of uncertainty in the derived eccentricities and arguments of periastron. With the results of equations 1 and 2, we calculate the eccentricity, e . Using equation 1 at two different eclipses, we measure $\frac{d}{dt} (e \cos \omega)$, which can also be written as

$$\frac{d}{dt} (e \cos \omega) = -e\dot{\omega} \sin(\omega). \quad (3)$$

Rearranging gives

$$\dot{\omega} = \frac{d}{dt} (\cos \omega) \frac{1}{\sin \omega}. \quad (4)$$

Here, we assume that the eccentricity e remains approximately constant over the TESS observational baseline. This is generally a good approximation for hierarchical triples, where the apsidal precession timescale is much shorter than the eccentricity modulation timescale. However, perturbations from a third body can in principle induce measurable changes in e over multi-year baselines (e.g. McKee & Montet 2023), so this assumption introduces an additional (usually small) systematic uncertainty.

The measured $\dot{\omega}$ therefore reflects the combined contributions from GR, tides and rotation, and any additional precession induced by a third body, all of which are additive. Thus, the precession due to a third body would be the difference between the total observed precession and that induced by tides and GR:

$$\dot{\omega}_{3rd} = \dot{\omega} - \dot{\omega}_{GR} - \dot{\omega}_{CL} \quad (5)$$

where $\dot{\omega}_{GR}$ and $\dot{\omega}_{CL}$ are the precession due to GR and classical (tidal and rotational) effects, respectively. The precession due to GR, following Gimenez (1985), can be written as:

$$\dot{\omega}_{GR} = (5.447127276 \times 10^{-4}) \left(\frac{1}{1 - e^2} \right) \left(\frac{M_1 + M_2}{P} \right)^{\frac{2}{3}} \text{ deg cycle}^{-1}. \quad (6)$$

M_1 and M_2 are the masses of the primary star and secondary star, respectively, in units of solar masses, and P in units of days. As we only select systems which have been identified as main-sequence binaries, we use temperature values from Stassun et al. (2019) and temperature-mass relations from Eker et al. (2018) to determine the masses of the stars in the binary. Precession due to tidal and rotational effects, following Baroch et al. (2021), can be represented by:

$$\dot{\omega}_{CL} = 360 \times \sum_{i=1}^2 \left(k_i c_i^{rot} + k_i c_i^{tid} \right) \text{ deg cycle}^{-1} \quad (7)$$

where k_i is the internal structure (or apsidal) constant (Claret & Gimenez 1993), which describes how mass is distributed inside a star; a star with centrally concentrated mass has a small k (< 0.02), whereas a star with a more uniform mass distribution has a larger k (> 0.1). We adopt $k_i = 0.01$ as is used in the work of Kostov et al. (2021), adapted from the work of Torres et al. (2010) as an average value of the term for main sequence stars. The rotational term, c_i^{rot} , following Baroch et al. (2021), is calculated as:

$$c_i^{rot} = \frac{r_i^5}{(1 - e)^2} \left(1 + \frac{M_{3-i}}{M_i} \right) \left(\frac{\Omega_i}{\Omega_m} \right)^2 \quad (8)$$

Ω_i and Ω_m are the angular velocity of the star’s rotation and the angular velocity of its orbital motion, respectively. Tidal theory and observations both show that binaries with periods $\lesssim 10 - 12$ days are typically synchronised (Zahn 1977; Meibom & Mathieu 2005). We therefore assume $\Omega_i = \Omega_m$. r_i is the ratio of the star’s radius to the semimajor axis of its orbit, where the radius is determined using temperature-radius relations from Eker et al. (2018) and the semimajor axis is determined through Kepler’s 3rd law and our precise determination of the binary’s orbital period. The tidal term, c_i^{tid} , following Baroch et al. (2021), can be expressed as:

$$c_i^{tid} = 15r_i^5 \frac{M_{3-i} (1 + 1.5e^2 + 0.125e^4)}{(1 - e^2)^5} \quad (9)$$

A positive $\dot{\omega}_{3rd}$ value indicates that there is precession consistent with an additional perturbation caused by a third body in the system orbiting the EB. We classify the remaining systems with a positive $\dot{\omega}_{3rd}$ as candidate EBs to host a third body companion.

2.7 Defining Parameter Space of Third Body

The value of $\dot{\omega}_{3rd}$ allows us to determine the allowed parameter space for the mass and semimajor axis of the third body, following Miralda-Escudé (2002) using:

$$\dot{\omega}_{3rd} = 360 \left(\frac{3M_3 a^3}{4(M_1 + M_2) a_3^3} \right) \text{ deg cycle}^{-1} \quad (10)$$

where a is the semimajor axis of the binary star, a_3 is the perturber's semimajor axis, and M_3 is the mass of the perturber. We are especially interested in the region just outside the binary's critical stability radius, given the high abundance of CBPs residing in this area. This radius, from [Holman & Wiegert \(1999\)](#), can be expressed as:

$$r_{crit} = a(1.6 + 5.1e - 2.22e^2 + 4.12\mu - 4.27e - 5.09\mu^2 + 4.61e^2\mu^2) \quad (11)$$

where μ and e are the binary's mass ratio, $M_2/(M_1 + M_2)$, and eccentricity, respectively. The perturber could fall anywhere along the blue curve defined by Figure 4 outside of the critical radius. The lower mass limit, $M_{3,min}$, is then determined as the point where the perturber parameter curve (blue line) intersects the critical radius (right edge of grey shaded region). The upper mass limit is poorly constrained at this point, but will be refined in future work (see Section 4.6 for more details).

3 RESULTS

We visually inspect the O-C and folded light curve plots of the 1,590 remaining systems and identify 71 as exhibiting evidence of apsidal precession. After subtracting the terms $\dot{\omega}_{GR}$ and $\dot{\omega}_{CL}$, 36 EBs remain with precession that cannot be accounted for by GR and tidal/rotational effects, outlined in Table 1.

We also note 31 systems revealing evidence of the light travel time effect (LTTE); we provide the TIC ID's and semi-amplitude values of the LTTE signal in Table 2. Otherwise known as the Rømer Delay ([Rømer 1677](#)), LTTE is the observed shift in timing of both eclipses due to a change in the light's path length to Earth as the barycentre of the binary wobbles around due to a third companion. Detectable LTTE in such cases would likely be caused by brown dwarf, stellar, or higher mass companions. Although these are interesting, the results of this paper focus on possible planet-mass companions. Thus, we focus on the 36 EBs in Table 1.

TIC 84546771 and TIC 198242678 both show signals that resemble fast, shorter-term precession likely caused by a more massive companion. TIC 115396972 is likely to have non-planetary-mass companions, as the minimum perturber mass lies right on the upper limit of a brown dwarf mass. We also exclude TIC 444544588 and TIC 167756615 due to their renormalised unit weight error (RUWE) from Gaia ([Gaia Collaboration 2020](#)). A high RUWE value ($> \sim 1.4$) suggests that the star's motion is not well described by a single-star model, which is often a sign of an unresolved companion inducing detectable photocentre motion. For the systems in our sample, planet-mass companions at circumbinary separations near the stability limit are expected to induce astrometric signals far below Gaia's detection threshold (typically tens of μas , [Perryman 2011](#); [Gaia Collaboration et al. 2016](#)). Thus, Gaia RUWE is not sensitive to the types of CBPs we aim to detect. Likewise, the inner binaries themselves are unlikely to contribute significantly to the RUWE since the binaries we are looking at produce photocentre motions that are below Gaia's resolution and are effectively averaged out over the mission baseline ([Stassun & Torres 2021](#)). The RUWE for TIC 444544588 and TIC 167756615 are 2.45 and 2.23, respectively; therefore, they are likely to have a more massive companion. Although TIC 441496809, TIC 165615442, TIC 121092916, and TIC 342356517 exhibit apsidal precession consistent with a potential planetary-mass tertiary companion, their measured precession rates are all below a 3σ significance threshold. As such, we do not consider them candidates at

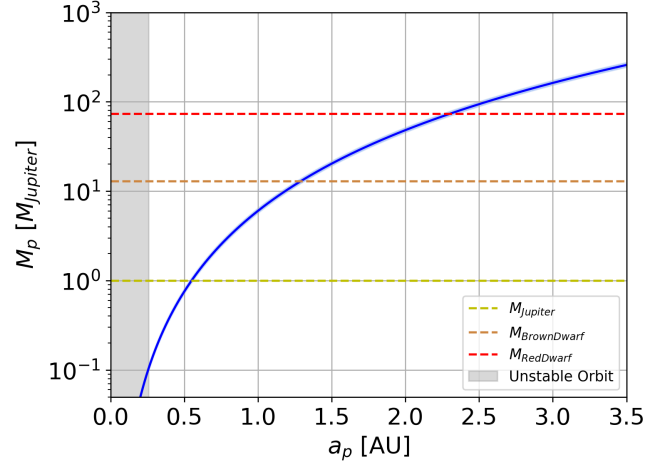


Figure 4. The parameter space for the companion to TIC 286310830, represented by the blue line. This precession could be due to a $\sim 0.15M_{Jupiter}$ companion at ~ 0.25 AU. The region within the critical stability radius is shaded in grey.

this stage. Additional eclipse timing is required to confirm whether these systems host third bodies; for that reason, we exclude them from our candidate count. We therefore present 27 candidate circumbinary planets, with more than half permitting the existence of sub-Jupiter mass objects.

The O-C plots for the systems from Table 1 are shown in Figures A1 - A5, where Figures A4 and A5 show the systems with short-term variations in the O-C plot. The mass vs. semimajor axis plots are shown in Figures A6 - A8.

We test the methods on TIC 172900988, the EB discussed above with a known CBP and observed apsidal precession. Our analysis resulted in a $\dot{\omega}_{3rd}$ of $2.41 \pm 0.11 \times 10^{-3}$ degrees per cycle compared to the estimate of 2.71×10^{-3} degrees per cycle from [Kostov et al. \(2021\)](#). Considering the full apsidal period is ~ 50 years, we expect a $\sim 10\%$ discrepancy between the two calculations due to a change in phase of $\cos \omega$ between these observations and the 2006-2021 observations used in that paper. This test validates the methods used to detect and quantify apsidal precession.

4 DISCUSSION

In this work, we demonstrate that we can detect apsidal precession of EBs at a level of precision that enables the detection of sub-Jovian mass planets. We identify 27 systems that could host a planetary mass perturber, with over half allowing for sub-Jupiter mass. If the general population follows trends of the known CBPs, we can infer that the tertiary companions are likely to exist just outside of the critical radius of the binary. In this case, all 27 systems could be confirmed as CBPs. Refining the mass to rule out higher-mass companions is required for confirmation and relies on attaining RV data (see Section 4.6 for more information).

4.1 Comparison to the Known CBP Population

The 27 candidates identified in this work differ in several ways from the currently known CBPs discovered via transits. Transit surveys preferentially detect systems with cool, low-luminosity primaries, long eclipse durations, and deep transits; these biases make CBP

TIC ID	P [days]	$\dot{\omega}_{\text{obs}}$ [10^{-3} deg/cycle]	$\dot{\omega}_{\text{GR}}$ [10^{-3} deg/cycle]	$\dot{\omega}_{\text{CL}}$ [10^{-3} deg/cycle]	$\dot{\omega}_{\text{3rd}}$ [10^{-3} deg/cycle]	$M_{3,\text{min}}$ [M_{Jup}]
81741369	10.0920 ± 0.0001	0.84 ± 0.01	0.253 ± 0.009	0.02 ± 0.01	0.57 ± 0.02	0.101 ± 0.003
293225466	129.3214 ± 0.0008	13.3 ± 0.7	0.036 ± 0.002	0.000 ± 0.000	13.3 ± 0.7	1.43 ± 0.08
274182408	6.554 ± 0.001	1.8 ± 0.1	0.26 ± 0.01	0.06 ± 0.05	1.5 ± 0.1	0.19 ± 0.01
457579488	14.6925 ± 0.0005	0.48 ± 0.02	0.182 ± 0.008	0.01 ± 0.01	0.28 ± 0.02	0.038 ± 0.003
124282654	11.3293 ± 0.0002	2.8 ± 0.2	0.172 ± 0.008	0.008 ± 0.009	2.6 ± 0.2	0.29 ± 0.03
286310830	8.3687 ± 0.0003	1.12 ± 0.07	0.22 ± 0.01	0.02 ± 0.02	0.87 ± 0.08	0.109 ± 0.009
51629874	6.465 ± 0.001	14.7 ± 1.4	0.23 ± 0.04	0.04 ± 0.04	14.4 ± 1.4	1.5 ± 0.1
123951716	23.1065 ± 0.0003	1.1 ± 0.1	0.136 ± 0.006	0.003 ± 0.002	1.0 ± 0.1	0.14 ± 0.01
396170777	6.5656 ± 0.0002	1.3 ± 0.1	0.25 ± 0.01	0.05 ± 0.04	1.0 ± 0.1	0.12 ± 0.02
139699256 ¹	5.952 ± 0.001	1.3 ± 0.1	0.29 ± 0.01	0.07 ± 0.04	1.0 ± 0.1	0.14 ± 0.02
56023695	8.177 ± 0.002	27.3 ± 2.7	0.39 ± 0.01	1.2 ± 0.7	25.7 ± 2.8	5.0 ± 0.5
292357653	23.1476 ± 0.0002	0.507 ± 0.009	0.15 ± 0.01	0.02 ± 0.03	0.34 ± 0.03	0.040 ± 0.004
82893635	28.5504 ± 0.0007	0.76 ± 0.07	0.13 ± 0.01	0.01 ± 0.01	0.61 ± 0.07	0.084 ± 0.009
196989952	7.281 ± 0.002	2.57 ± 0.03	0.42 ± 0.01	0.4 ± 0.2	1.7 ± 0.2	0.27 ± 0.04
146204045 ¹	14.192 ± 0.001	7.2 ± 0.8	0.205 ± 0.006	0.005 ± 0.003	7.1 ± 0.8	1.3 ± 0.2
283651681	7.62 ± 0.02	1.1 ± 0.1	0.24 ± 0.01	0.03 ± 0.03	0.8 ± 0.1	0.11 ± 0.02
61656788	4.3028 ± 0.0007	1.79 ± 0.03	0.42 ± 0.01	0.2 ± 0.1	1.1 ± 0.1	0.19 ± 0.02
444544588	16.349 ± 0.002	24.3 ± 3.1	0.25 ± 0.01	0.11 ± 0.06	23.9 ± 3.1	4.8 ± 0.6
252497283	5.04 ± 0.01	2.7 ± 0.3	0.30 ± 0.01	0.1 ± 0.1	2.2 ± 0.3	0.28 ± 0.04
167699456	18.74 ± 0.01	4.0 ± 0.6	0.11 ± 0.01	0.003 ± 0.008	3.9 ± 0.6	0.39 ± 0.06
343127696	4.672 ± 0.002	22.2 ± 3.5	0.31 ± 0.01	0.2 ± 0.1	21.7 ± 3.5	2.4 ± 0.4
253270207	6.11 ± 0.01	5.1 ± 0.5	0.34 ± 0.01	0.9 ± 0.5	3.8 ± 0.7	0.6 ± 0.1
158330804 ¹	11.355 ± 0.002	0.61 ± 0.03	0.205 ± 0.008	0.09 ± 0.06	0.32 ± 0.07	0.041 ± 0.009
115396972	19.809 ± 0.001	64 ± 17	0.18 ± 0.01	0.03 ± 0.02	64 ± 17	10.0 ± 0.2
399127035	5.448 ± 0.001	8.8 ± 2.4	0.26 ± 0.01	0.1 ± 0.1	8.5 ± 2.4	0.9 ± 0.3
355503224	6.9247 ± 0.0002	0.8 ± 0.1	0.26 ± 0.01	0.04 ± 0.02	0.5 ± 0.1	0.07 ± 0.02
95622298	4.5123 ± 0.0003	5.9 ± 1.6	0.32 ± 0.01	0.1 ± 0.1	5.4 ± 1.6	0.6 ± 0.2
64366964 ¹	4.459 ± 0.003	11.5 ± 0.7	0.49 ± 0.01	5.9 ± 1.5	5.0 ± 1.6	0.8 ± 0.3
198242678	4.6298 ± 0.0009	65 ± 22	0.27 ± 0.01	0.3 ± 0.3	64 ± 22	6.1 ± 2.0
84546771	4.2837 ± 0.0009	42 ± 14	0.37 ± 0.01	0.2 ± 0.1	41 ± 14	5.7 ± 1.7
291751499	5.1957 ± 0.0003	16.2 ± 5.7	0.30 ± 0.01	0.11 ± 0.08	15.8 ± 5.7	1.8 ± 0.8
167756615	19.181 ± 0.007	15.8 ± 5.8	0.12 ± 0.01	0.001 ± 0.001	15.7 ± 5.8	1.8 ± 0.6
441496809	5.7542 ± 0.0008	4.8 ± 1.9	0.26 ± 0.01	0.08 ± 0.09	4.4 ± 1.9	0.5 ± 0.2
165615442	5.475 ± 0.001	13.0 ± 6.0	0.27 ± 0.01	0.08 ± 0.09	12.6 ± 6.0	1.3 ± 0.6
121092916	8.2198 ± 0.0002	7.0 ± 4.3	0.21 ± 0.01	0.02 ± 0.02	6.7 ± 4.3	0.7 ± 0.4
342356517	11.9666 ± 0.0009	1.9 ± 1.4	0.158 ± 0.008	0.008 ± 0.009	1.8 ± 1.4	0.2 ± 0.1

¹ Systems which also exhibit the LTTE.**Table 1.** Period, apsidal precession contributions, and minimum perturber mass for all precessing systems. Rows are sorted by descending $\dot{\omega}_{\text{3rd}}/\sigma_{\dot{\omega}_{\text{3rd}}}$. The period is the average of the primary and secondary period.

discoveries strongly skewed towards Sun-like or cooler binaries. In contrast, our precession-based method is largely insensitive to stellar radius, luminosity, or transit depth. As a result, our sample includes a broader range of stellar types, including a fraction of hotter and larger systems for which transit detection would be extremely challenging. There are no known CBPs discovered by the transit method orbiting stars hotter than 6400 K, while 30% of our candidates are: the hottest stars in our sample have effective temperatures over 9000 K. Additionally, the EBs in our sample have a wider range of orbital periods than the EBs with known CBPs: our shortest system has an orbital period of 4.2837 ± 0.0009 days, while our longest has a period of 129.3214 ± 0.0008 days, both outside of the range of periods of confirmed transiting planet-hosting CBPs. A full demographic comparison (distributions of perturber mass, inclination, etc.) is beyond the scope of this work but will be presented in future analyses.

4.2 LTTE and Precession

TIC 158330804, TIC 139699256, TIC 64366964, and TIC 146204045 show signs of LTTE in addition to the diverging pre-

cession signal in their O-C diagrams (see Table 2 for semi-amplitude estimates). This double effect may be particularly informative, because the combination of apsidal precession and LTTE provides complementary constraints that can help break degeneracies in the inferred mass and orbital configuration of the tertiary companion. In principle, LTTE and apsidal precession could be produced by the same object or by two independent companions. Wider-baseline data or dynamical modelling is ultimately required to confirm or rule out multi-perturber configurations.

4.3 Short Term Variation

TIC 84546771 and TIC 198242678 both show short-term variations that require more follow-up to determine the cause of such precession. Possible causes of these signals include a very massive or nearby object. In both cases, the rapid evolution of the O-C curve suggests a dynamical influence that cannot be fully characterised with the current data. Continued timing monitoring and spectroscopic follow-up will be essential to determine whether these variations arise from a

TIC ID	Semi-Amplitude [min]	TIC ID	Semi-Amplitude [min]
280625073	4	243588685	4
360088090	2	445259184	3
9655156	5	225138160	5
447423507	0.75	279638469	5
407027744	2	361887558	2
301260701	3	81923827	1
276471941	3	265338722	3
160676497	4	236212010	2
293271277	4	418011373	5
245217638	5	64355437	2
165295354	3	265288713	2
436131579	6	359960689	6
279647970	1.5	157089542	1.5
407165593	3	45637974	1
144215102	2.5	311706965	4
220113185	2.5	158330804	0.25
139699256	2	64366964	5
14620404	8		

Table 2. The EBs that exhibit signs of the LTTE. The semi-amplitudes are all estimates; follow-up modelling and data are required for these systems. The last five on this list also exhibit precession signals; the observed precession of TIC 157089542 can all be accounted for by GR and tides, whereas the remaining four likely have a perturber.

compact tertiary companion, dynamical interactions within a hierarchical system, or an alternative solution.

Short-term apsidal variation of this kind can be produced by (1) a massive tertiary on a moderately eccentric orbit, (2) resonant hierarchical architectures, or (3) combinations of multiple low-mass perturbers whose interactions are nonlinear over the TESS baseline. These systems are therefore strong candidates for full N-body dynamical modelling, but such work requires more precise constraints on the binary parameters. Future RV measurements and extended eclipse timing baselines are essential to determine whether these are unusual CBP configurations or more complex hierarchical triples.

4.4 Low-Mass Cases

The methods developed here allow for the detection of tertiary companions down to sub-Neptune masses. For several systems, specifically TIC 457579488, TIC 292357653, TIC 355503224, and TIC 158330804, the intersection of the perturbers allowed parameter space with the system’s critical radius permits solutions involving companions less massive than Neptune. A circumbinary planet of this mass would be the least massive detected to date, placing these systems at the frontier of current sensitivity limits. Continued monitoring and complementary follow-up observations are crucial for confirming such low-mass candidates and refining their orbital properties.

A natural question is whether these low-mass candidates are detectable through radial velocities alone. For a sub-Neptune mass CBP orbiting just outside the critical radius (typically 0.3–0.6 AU), the reflex velocity amplitude of the binary barycentre is not more than a few m s^{-1} , even if the system is edge on. This magnitude places these planets near the limit of current state-of-the-art precision for surveys of bright systems such as BEBOP (Martin et al. 2019). Thus, RVs may be able to place meaningful upper limits, but unambiguous planet detection may require a combination of long-baseline ETV monitoring, dynamical modelling, and astrometric constraints from future Gaia releases.

4.5 Mass–Separation Limits and Companion Types

Apsidal precession places limits on the mass–semimajor axis relationship of permitted companions, with the required mass to induce the observed precession growing as a^3 . Stellar tertiaries beyond a few AU would, if sufficiently massive, outshine the binary and be easily identified spectroscopically. Gaia astrometry already constrains the presence of stellar or brown-dwarf companions for many systems, and Gaia DR4 will significantly tighten these limits.

While our analysis assumes main-sequence tertiary companions, compact objects (white dwarfs, neutron stars, black holes) could in principle produce similar dynamical signatures. Most such companions at the relevant separations would produce detectable RV accelerations or Gaia astrometric motion. Future observations will help determine whether any observed precession is caused by such compact objects.

4.6 Future Work

The 27 CBP candidates require follow-up radial velocity observations to refine their mass estimates and to rule out brown dwarf or stellar-mass tertiaries. All candidates are bright enough ($T < 13.5$) for precise RV follow-up with modern 4–10 m class spectrographs, similar to those used in recent circumbinary RV surveys such as BEBOP and related programs. These systems therefore represent promising targets for future observing campaigns rather than relying on specific facility commitments.

Considering the sample we analysed was only a small fraction of the 2 million EBs in Gaia’s catalogue (Mowlavi et al. 2023), we anticipate many more detections as we expand this search across the larger sample. Additionally, combining the 7 year TESS data with past and future missions will increase the baseline of the search, and thus the sensitivity to small companions. Longer baselines will not only improve constraints on apsidal precession but also allow for the identification of multi-perturber systems and time-variable dynamical regimes that are currently indistinguishable within the existing data. Also, an in-depth transit search may find companions in these systems, making follow-up more straightforward. The combi-

nation of RVs, eclipse timing, Gaia astrometry, and systematic transit searches has the potential to transform the circumbinary companion population from a handful of transiting planets to a statistically meaningful, dynamically rich sample.

5 CONCLUSIONS

Upon initial inspection of 1,590 eclipsing binaries from Gaia's catalogue of over 2 million systems, we present 71 EBs that show signs of precession, 36 of which cannot be accounted for by effects due to general relativity and the rotational/tidal effects of the stars themselves. The calculation of precession was based on the change in the argument of periastron over time of the binary star, which can be determined by the exact timing of both primary and secondary eclipses. 27 of the 36 EBs may host a planet-mass companion in an outer orbit. We therefore present the discovery of 27 circumbinary planet candidates that induce apsidal precession on their host binary. Once further analysis is conducted to determine the perturber mass, we can confirm them as CBPs.

This method allows for the possibility of multiplying the number of known circumbinary planets because it is not limited in the orientation of the planet. It has the capability of detecting CBPs with higher mutual inclinations, therefore extending the sample to diverse architectures and orbital geometries. The findings of this work will allow us to robustly test formation theories, constrain migration histories, and understand long-term evolution of circumbinary systems.

ACKNOWLEDGEMENTS

The authors wish to express their gratitude to the TESS Mission team, the Quick-Look Pipeline developers, and the Gaia project scientists and operations teams, whose dedicated efforts in producing and maintaining high-quality photometric and astrometric data have made this work possible. We are also grateful to our collaborators for their willingness to support and contribute to the follow-up observations associated with this project.

This paper includes data collected by the TESS mission and processed by the Science Processing Operations Center. Funding for the TESS mission is provided by the NASA Science Mission Directorate. This research has made use of data products from the Gaia mission, funded by the European Space Agency (ESA), and of resources hosted at the Mikulski Archive for Space Telescopes (MAST), operated by the Space Telescope Science Institute under NASA contract NAS5-26555.

M.T. acknowledges support from the University of New South Wales through the undergraduate University International Postgraduate Award and the Burbage Astronomy Student Fund.

DATA AVAILABILITY

The data underlying this article are publicly available. TESS light curves and associated data products can be accessed through MAST. Gaia astrometric and photometric data are available through the ESA Gaia Archive. All additional data or analysis products used in this study will be shared upon reasonable request to the corresponding author.

REFERENCES

- Abod C. P., Chen C., Smallwood J. L., Rabago I., Martin R. G., Lubow S. H., 2022, *Monthly Notices of the Royal Astronomical Society*, 517, 732
- Baroch D., Giménez A., Ribas I., Morales J. C., Anglada-Escudé G., Claret A., 2021, *A&A*, 649, A64
- Baycroft T. A., et al., 2025, *MNRAS*, 541, 2801
- Bennett D. P., et al., 2016, *AJ*, 152, 125
- Borucki W. J., et al., 2010, *Science*, 327, 977
- Charbonneau D., et al., 2005, *ApJ*, 626, 523
- Chen C., Franchini A., Lubow S. H., Martin R. G., 2019, *Monthly Notices of the Royal Astronomical Society*, 490, 5634
- Chen C., Martin R. G., Lubow S. H., Nixon C. J., 2024, *ApJ*, 961, L5
- Claret A., Gimenez A., 1993, *A&A*, 277, 487
- Coleman G. A. L., 2024, *MNRAS*, 530, 630
- Cowling T. G., 1938, *MNRAS*, 98, 734
- Doyle L. R., et al., 2011, *Science*, 333, 1602
- Einstein A., 1916, *Annalen der Physik*, 354, 769
- Eker Z., et al., 2018, *MNRAS*, 479, 5491
- Foucart F., Lai D., 2013, *The Astrophysical Journal*, 764, 106
- Franchini A., Lubow S. H., Martin R. G., 2019, *The Astrophysical Journal Letters*, 880, L18
- Gaia Collaboration 2020, VizieR Online Data Catalog: Gaia EDR3 (Gaia Collaboration, 2020), VizieR On-line Data Catalog: I/350. Originally published in: 2021A&A...649A...1G, doi:10.26093/cds/vizie.1350
- Gaia Collaboration et al., 2016, *A&A*, 595, A2
- Gimenez A., 1985, *ApJ*, 297, 405
- Goldberg M., Fabrycky D., Martin D. V., Albrecht S., Deeg H. J., Nowak G., 2023, *MNRAS*, 525, 4628
- Harrington R. S., 1968, *AJ*, 73, 190
- Hilditch R. W., 2001, *An Introduction to Close Binary Stars*
- Hipke M., Heller R., 2019, *TLS: Transit Least Squares*, Astrophysics Source Code Library, record ascl:1910.007 (ascl:1910.007)
- Holman M. J., Wiegert P. A., 1999, *AJ*, 117, 621
- Huang C. X., et al., 2020, *Research Notes of the American Astronomical Society*, 4, 204
- Kostov V. B., et al., 2020, *AJ*, 159, 253
- Kostov V. B., et al., 2021, *AJ*, 162, 234
- Kovács G., Zucker S., Mazeh T., 2002, *A&A*, 391, 369
- Levenberg K., 1944, *Quarterly of Applied Mathematics*, 2, 164
- Lightcurve Collaboration et al., 2018, *Lightcurve: Kepler and TESS time series analysis in Python*, Astrophysics Source Code Library (ascl:1812.013)
- Marquardt D. W., 1963, *Journal of the Society for Industrial and Applied Mathematics*, 11, 431
- Martin D. V., Triaud A. H. M. J., 2015, *MNRAS*, 449, 781
- Martin D. V., et al., 2019, *A&A*, 624, A68
- Mazeh T., Shaham J., 1979, *A&A*, 77, 145
- McKee B. J., Montet B. T., 2023, *AJ*, 165, 236
- Meibom S., Mathieu R. D., 2005, *ApJ*, 620, 970
- Miralda-Escudé J., 2002, *ApJ*, 564, 1019
- Mowlavi N., et al., 2023, *A&A*, 674, A16
- Newville M., et al., 2025, *LMFIT: Non-Linear Least-Squares Minimization and Curve-Fitting for Python*, doi:10.5281/zenodo.16175987
- Orosz J. A., et al., 2012a, *Science*, 337, 1511
- Orosz J. A., et al., 2012b, *ApJ*, 758, 87
- Perryman M., 2011, *The Exoplanet Handbook*
- Pierens A., Nelson R. P., 2013, *A&A*, 556, A134
- Prša A., et al., 2011, *AJ*, 141, 83
- Ricker G. R., et al., 2015, *Journal of Astronomical Telescopes, Instruments, and Systems*, 1, 014003
- Rømer O., 1677, *Philosophical Transactions of the Royal Society of London Series I*, 12, 893
- Schwamb M. E., et al., 2013, *ApJ*, 768, 127
- Standing M. R., et al., 2023, *Nature Astronomy*, 7, 702
- Stassun K. G., Torres G., 2021, *ApJ*, 907, L33
- Stassun K. G., et al., 2019, *AJ*, 158, 138
- Sterne T. E., 1939, *MNRAS*, 99, 451

Torres G., Andersen J., Giménez A., 2010, [A&ARv](#), **18**, 67
Virtanen P., et al., 2020, [Nature Medicine](#), **17**, 261
Welsh W. F., et al., 2012, [Nature](#), **481**, 475
Zahn J.-P., 1977, [A&A](#), **57**, 383

APPENDIX A: SUPPLEMENTAL FIGURES

This paper has been typeset from a \LaTeX file prepared by the author.

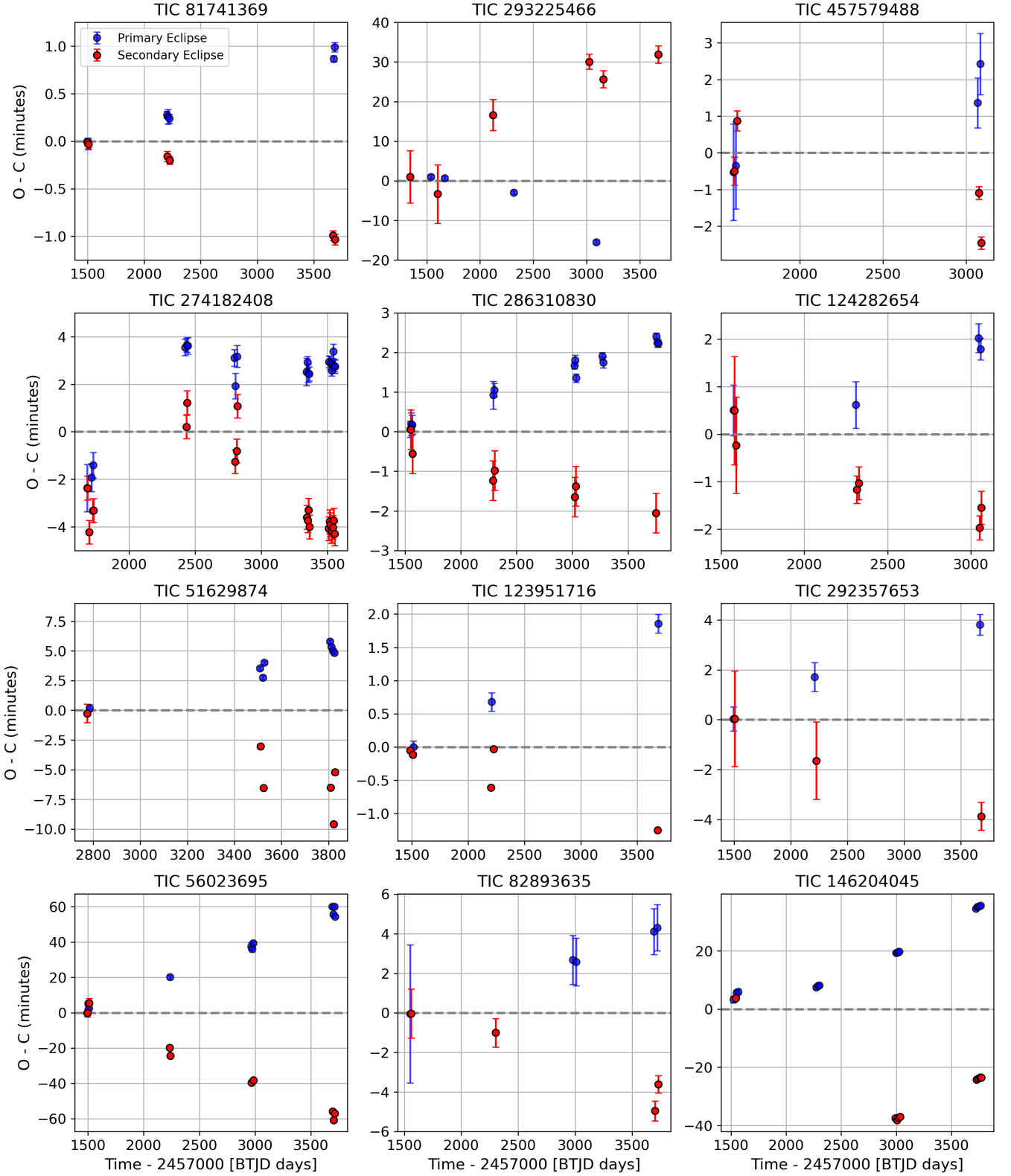


Figure A1. Same as Figure 3, but for the first dozen systems in Table 1.

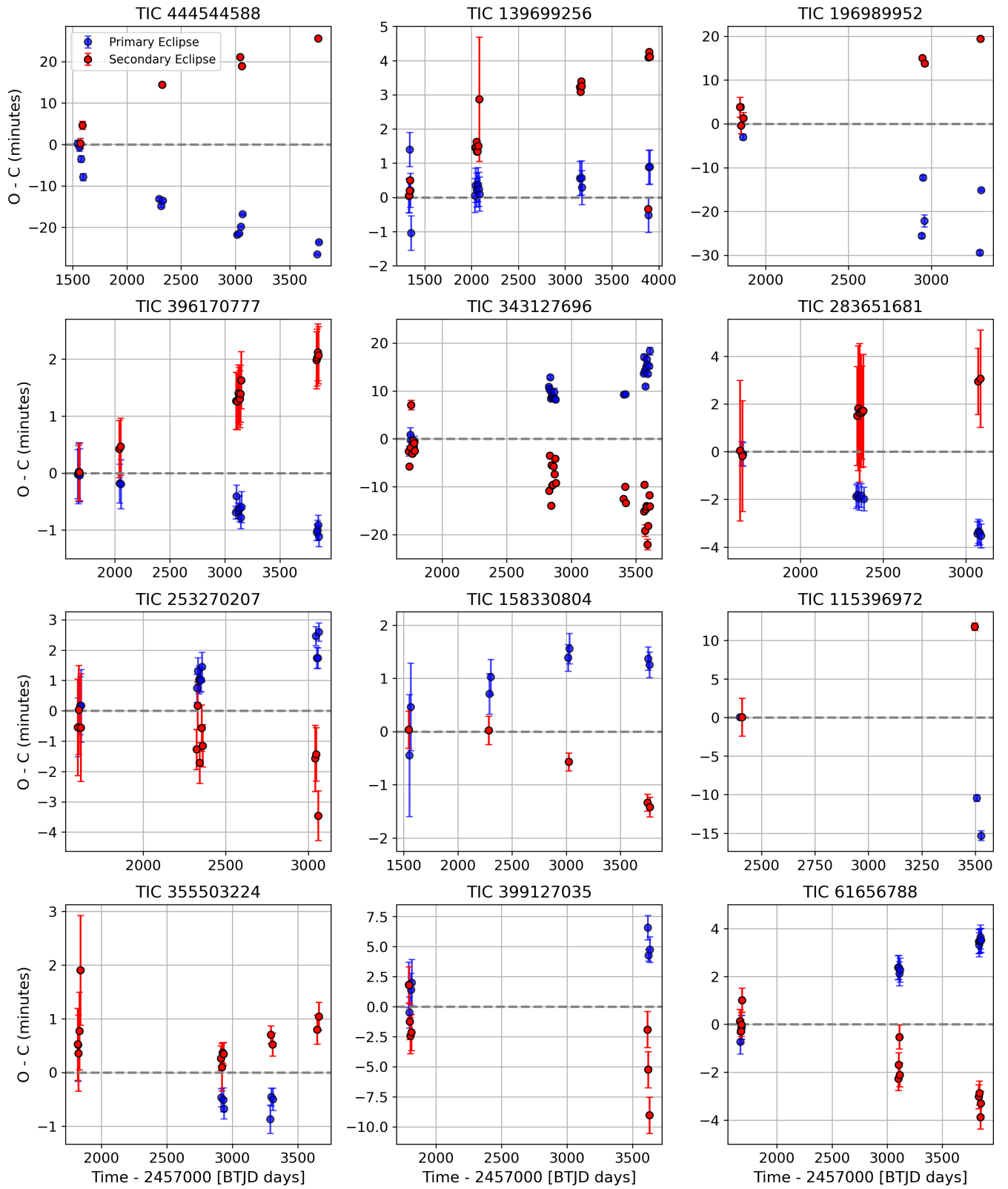


Figure A2. Same as Figure 3, but for the second dozen systems in Table 1.

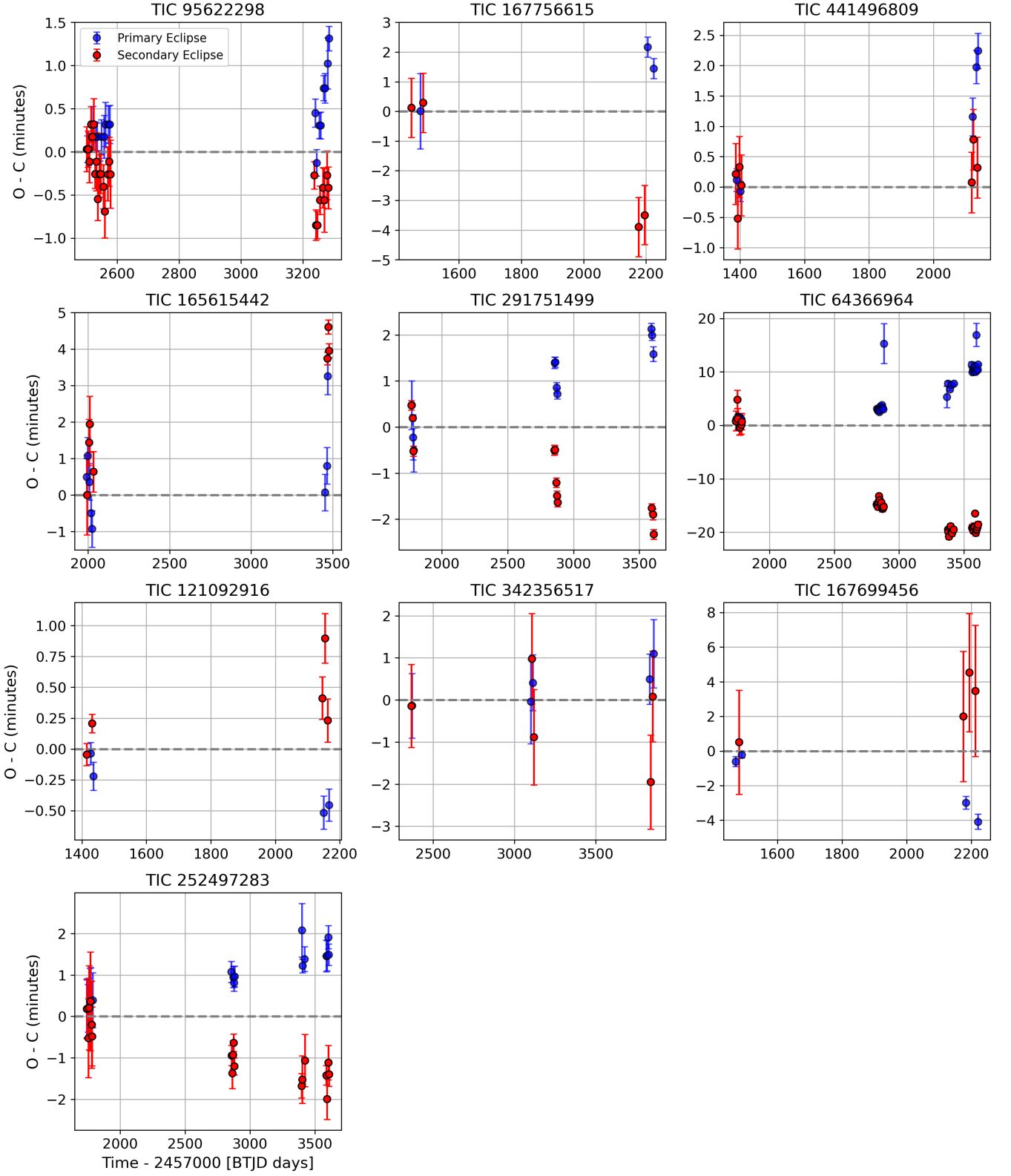


Figure A3. Same as Figure 3, but for the remaining systems in Table 1, excluding two that show short-term variation, displayed in Figures A4 and A5.

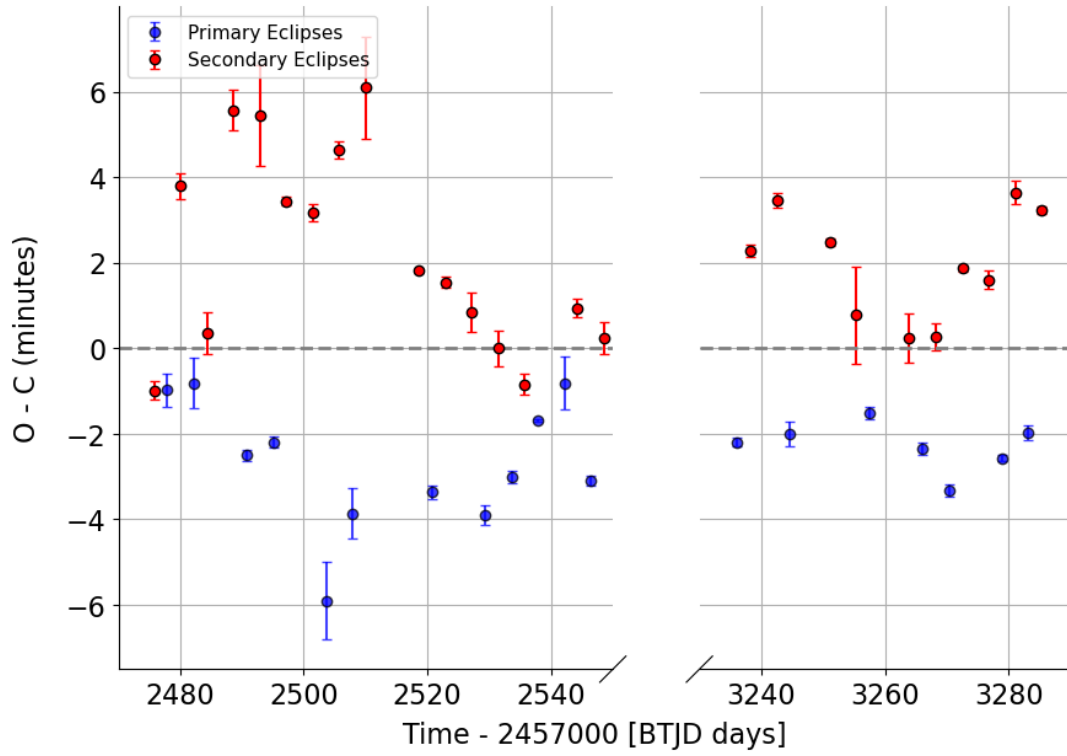


Figure A4. O-C plot of TIC 84546771, a ~ 4.28 -day EB showing short-term variation.

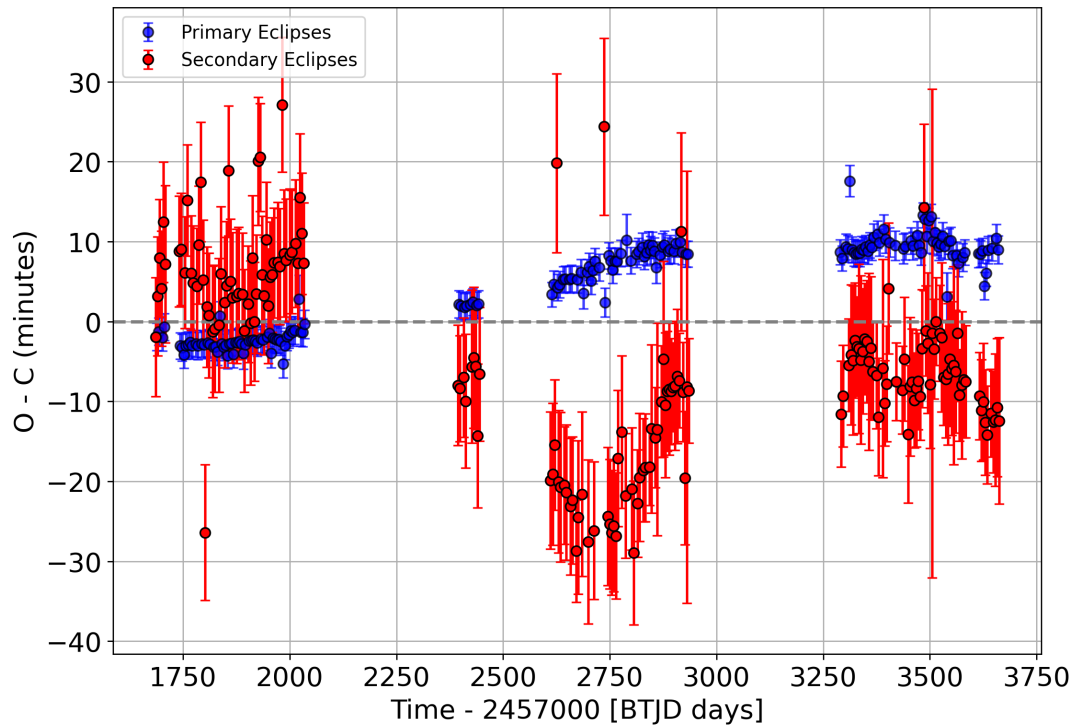


Figure A5. O-C plot of TIC 198242678, a ~ 4.63 -day EB showing short-term variation.

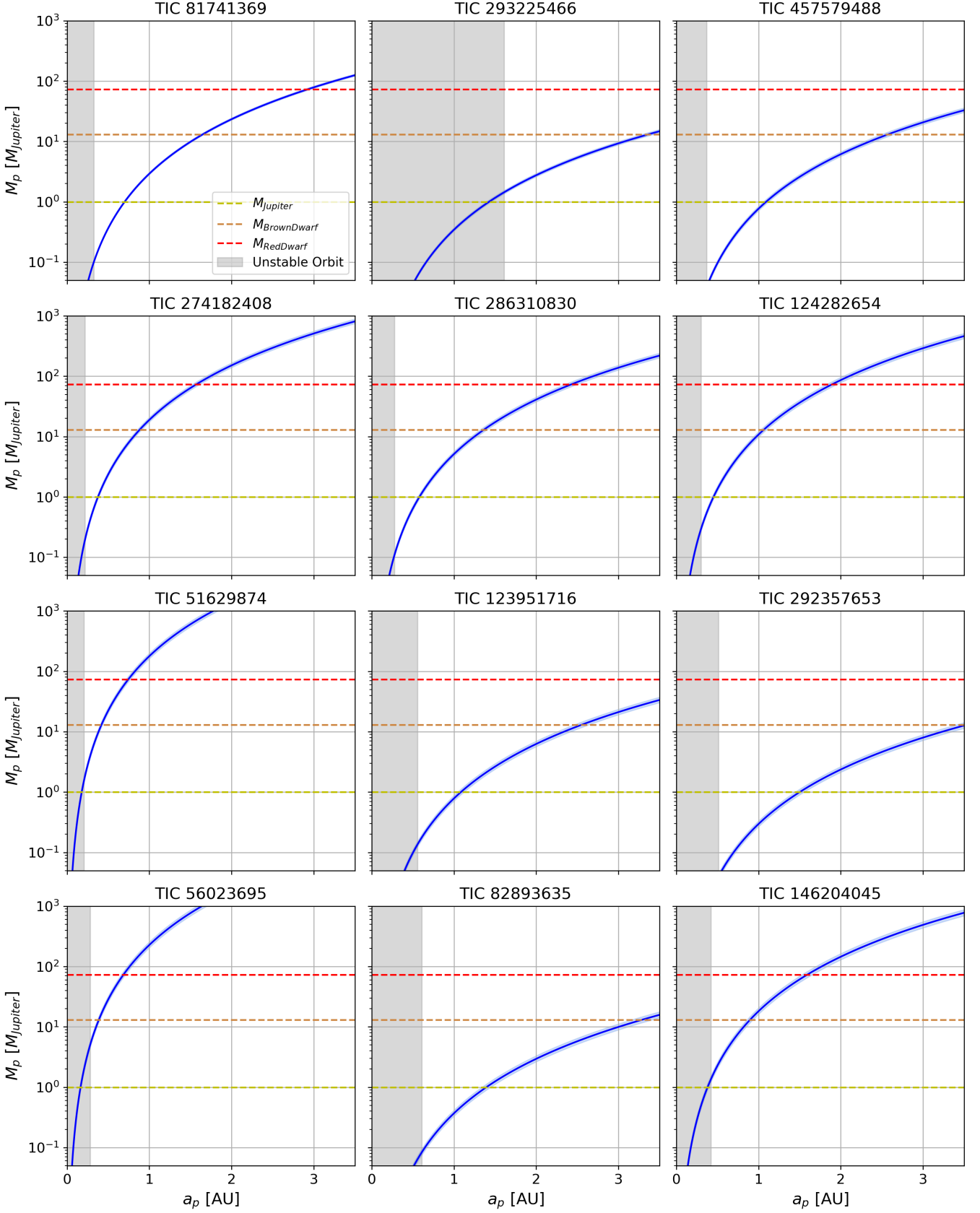


Figure A6. Same as Figure 4, but for the first dozen systems in Table 1.

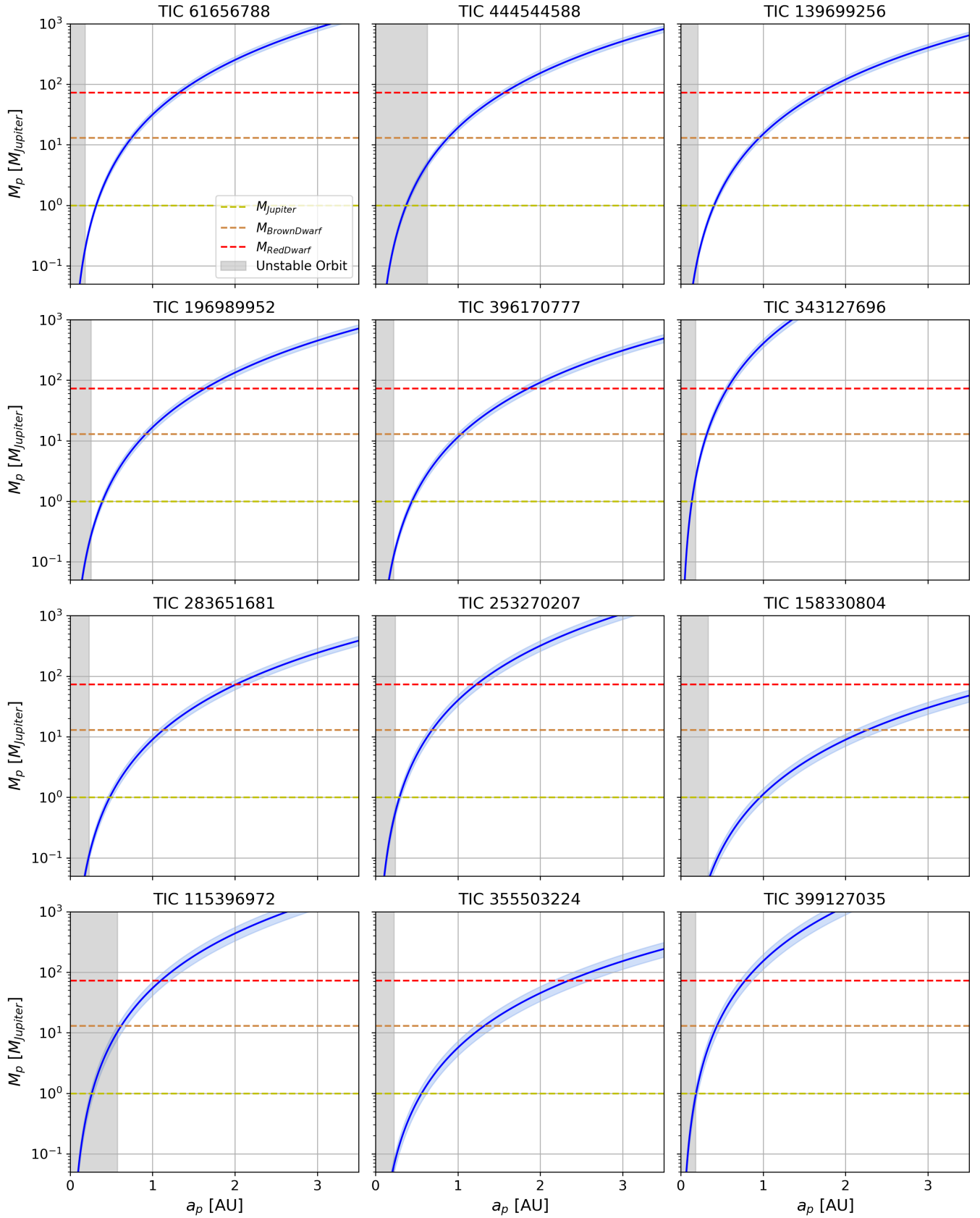


Figure A7. Same as Figure 4, but for the second dozen systems in Table 1.

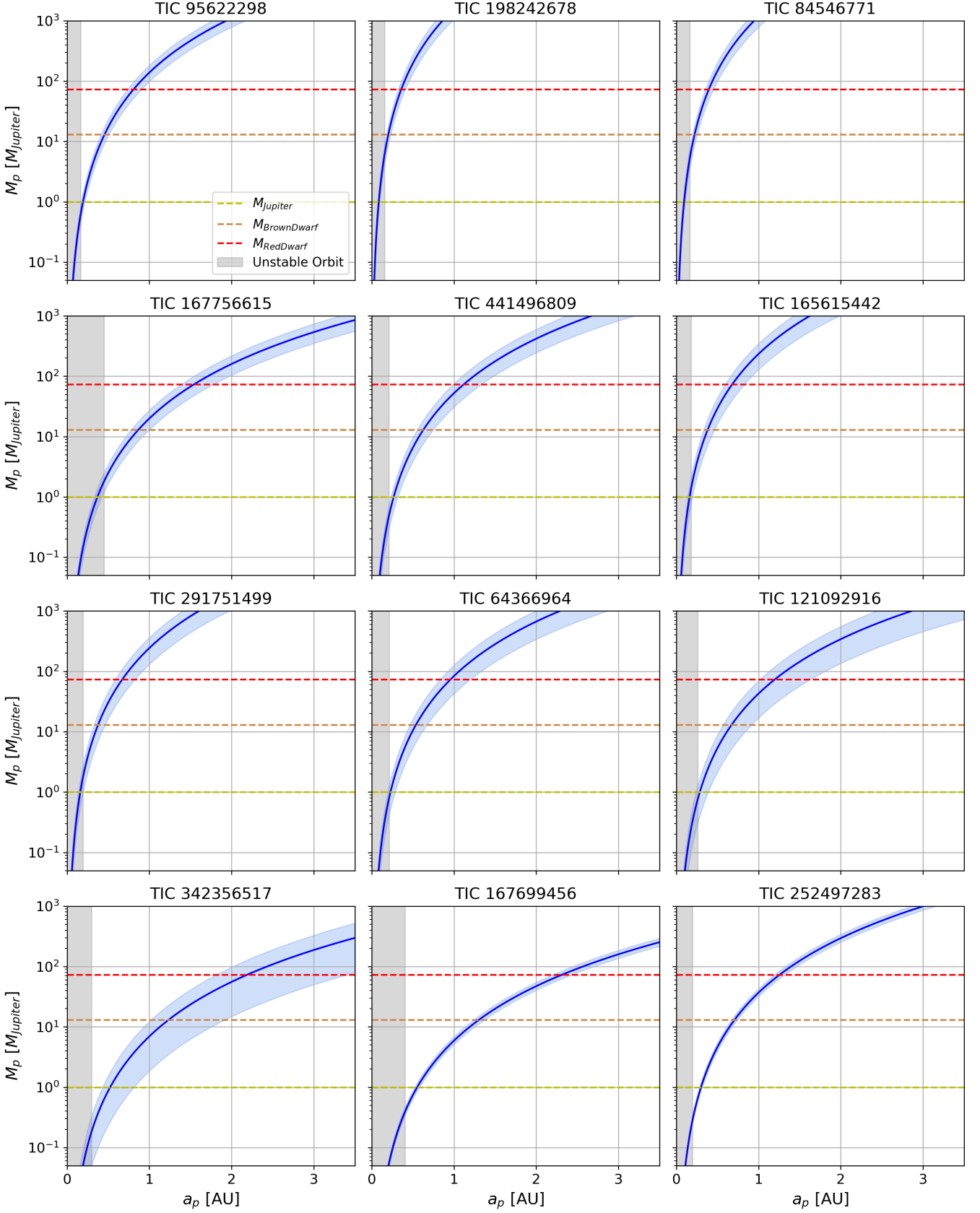


Figure A8. Same as Figure 4, but for the last dozen systems in Table 1.